Strauss, J.V., and Tosca, N.J., 2020, Mineralogical constraints on Neoproterozoic pCO2 and marine carbonate chemistry: Geology, v. 48, https://doi.org/10.1130/G47506.1

GSA DATA REPOSITORY 2020175

SUPPLEMENTARY GEOLOGICAL BACKGROUND

Callison Lake Formation, Yukon, Canada

The Callison Lake Formation of the Mount Harper Group (Windermere Supergroup) is widely exposed in the Coal Creek and Hart River inliers of the Ogilvie Mountains, Yukon, Canada (Fig. 1, main text). These strata have been subdivided into four informal members (Heterolithic, Talc, Ramp, and Transitional), which reflect different phases of mixed siliciclastic and carbonate sedimentation in a subtropical, restricted to open marine extensional basin formed during the break-up of Rodinia (Strauss et al., 2015). The Callison Lake Formation is bracketed in age between ca. 811 and 719 Ma by U-Pb chemical abrasion-isotope dilution-thermal ionization mass spectrometry (CA-ID-TIMS) dates on zircon from volcanic horizons in bounding strata (Fifteenmile Group and Mount Harper volcanic rocks, respectively) (Macdonald et al., 2010, 2018). Callison Lake strata are also temporally contained by two Re-Os depositional ages on organic-rich mudstones: 1) a 752.7 ± 5.5 Ma date from the Heterolithic-Talc member contact (Rooney et al., 2015), and 2) a 739.9 ± 6.1 Ma date from the middle portion of the Transitional member (Fig.1, main text; Strauss et al., 2014), making it one of the well-calibrated Tonian successions in the world.

Mg-silicates in the Callison Lake Formation occur as meter- to decameter-thick accumulations in the ~45–109 m-thick Talc member (Tosca et al., 2011; Strauss et al., 2015). These strata are mostly characterized by talc-rich black mudstone and diverse microbial dolostone facies deposited within a subtidal to supratidal depositional environment (Strauss et al., 2015). The Mg-silicates form stratiform cm- to m-thick intervals of talc-rich mudstone, drapes on stromatolitic laminae, and a wide variety of primary coated grains, such as ooids, oncolites, pisoids, and cortoids (Fig. 1, main text). Talc-rich intervals are occasionally capped by erosional surfaces where talc-rich mudstone is ripped-up to form cross-bedded intraclast dolowackestone or dolopackstone. The presence of sulfate evaporite pseudomorphs, tepees, mudcracks, and the intimate association of microbial dolostone and organic-rich fine-grained strata all indicate that Talc member strata were deposited in a periodically flooded tidal flat or sabkha (Strauss et al., 2015). A marine setting for these strata is also indicated by m-scale shoaling-upwards parasequences, as well as the presence of globally-recognized vase-shaped microfossils (Strauss et al., 2014; Cohen et al., 2017a) and unradiogenic Os_i isotopic data in Talc member mudstone (Strauss et al., 2014; Rooney et al., 2015).

Mg-silicates are absent in other siliciclastic and carbonate strata of the Callison Lake Formation, except in the form of rare drapes along stromatolitic bioherms in the Heterolithic and Transitional members (Strauss et al., 2015). Carbonate strata throughout the Callison Lake Formation are more commonly characterized by eponymous Neoproterozoic microbial fabrics, such as trap-and-bind stromatolites, microbialites, and oncolites, as well as thick accumulations of laminated to massive dolomudstone, dolowackestone, and dolograinstone dominated by ooids, intraclasts, and pisoids (Strauss et al., 2015). Despite evidence for evaporative carbonate sedimentation in the Callison Lake Formation, carbonate strata do not host evidence for precipitated fabrics, such as aragonite fans or microdigitate stromatolites, nor are there any notable accumulations of $CaCO_3$ microspar cements or molar-tooth structures.

Svanbergfjellet Formation, Nordhaustlandet and Ny Friesland, Svalbard, Norway

Neoproterozoic rocks exposed in northeastern Svalbard are part of the upper Hecla Hoek Series of the Northeastern basement province (Harland and Wilson, 1956; Wilson, 1958, 1961; Dallmann, 2015). The Hecla Hoek Series outcrop in nunataks and coastal sections in northeastern Spitsbergen and northwestern Nordaustlandet and is subdivided into the Veteranen, Akademikerbreen, and Polarisbreen groups (Fig. 1, main text). Whereas a different nomenclature has historically been used for strata exposed on the island of Nordaustlandet (Flood et al., 1969), correlation of these strata across Hinlopenstretet is unambiguous, and it has become the convention to use the better-known stratigraphic nomenclature from Spitsbergen when describing Neoproterozoic sedimentary rocks in northeastern Svalbard (Halverson et al., 2018a). This is important because Tosca et al. (2011) previously described Mg-silicates from the Hunnberg Formation (Flood et al., 1969), which is correlative with the Svanbergfjellet Formation (Fig. 1, main text; Harland and Wilson, 1956; Wilson, 1958, 1961; Knoll and Swett, 1990).

The ~2 km thick Akademikerbreen Group (Tonian) is almost exclusively composed of carbonate, and has been subdivided into the Grusdievbreen, Svanbergfjellet, Draken, and Backlundtoppen formations. The upper Grusdievbreen and lower Svanbergfjellet formations record the entirety of the ca. 810–800 Ma Bitter Springs carbon isotope excursion (Halverson et al., 2007, 2018a; Macdonald et al., 2010; Swanson-Hysell et al., 2015; Cohen et al., 2017b). The overlying Polarisbreen Group (specifically, the Russøya Member) preserves a negative $\delta^{13}C$ anomaly that was previously correlated with the so-called ca. 735 Ma Islay anomaly of Scotland (Hoffman et al., 2012; Rooney et al., 2014; Strauss et al., 2014; MacLennan et al., 2018). The basal Ediacaran Dracoisen cap dolostone occurs across the entire outcrop belt and serves as a useful chronostratigraphic marker (Harland et al., 1993; Halverson et al., 2004) that can be confidently assigned an age of ca. 635 Ma (Hoffmann et al., 2004; Condon, 2005; Calver et al., 2013).

The carbonate-dominated ca. 805–788 Ma Svanbergfjellet Formation (Halverson et al., 2018b) is subdivided into four members, which in stratigraphically-ascending order consist of the ~150 m-thick Lower Dolomite, ~150 m-thick Lower Limestone, ~120–150 m-thick Algal Dolomite, and ~70–150 m-thick Upper Limestone (Knoll and Swett, 1990). Dolostone-dominated strata of the Lower and Algal Dolomite members are characterized by interbedded stromatolitic boundstone, dolomudstone, intraclast packstone and wackestone, and dolograinstone with subordinate intervals of black to maroon mudstone. These strata record subtidal to peritidal sedimentation in a tidal flat to lagoonal depositional environment, as indicated by a combination of subaerial exposure indicators, such as mudcracks and tepees, as well as subtidal indicators including stromatolitic buildups, cross-bedded oolitic grainstones, and finely laminated carbonate and siliciclastic mudstones (Knoll and Swett, 1990; Maloof et al., 2006; Halverson et al., 2007). In contrast, limestone-dominated members of the Svanbergfjellet Formation are composed of dark grey to black, thin-bedded and planar- to wavy-laminated lime mudstone with abundant molar-tooth structures, which mostly reflect subtidal sedimentation in a shallow shelf to lagoonal depositional environment (Knoll and Swett, 1990).

Tosca et al. (2011) described nodular Mg-silicate occurrences associated with void-filling $CaCO_3$ microspar cements in stromatolitic and molar-tooth structures from both the Algal Dolomite and Upper Limestone members, which were previously misinterpreted as phosphate nodules (Knoll, 1984; Knoll and Swett, 1990). Our more recent observations of strata exposed at Roaldtoppen in Murchisonfjorden, Nordhaustlandet (Fig. DR1), suggest that Mg-silicates are also preserved in the Lower Dolomite Member, both in the form of cm- to m-thick talc-rich black mudstone deposits, as well as nodular and stratiform aggregates associated with $CaCO_3$ microspar

in lime mudstone, stromatolitic horizons, and molar-tooth structures (Fig. 2, main text; Fig. DR1). These Mg-silicate-rich strata are commonly reworked by current-generated structures, such as trough cross-stratification and hummocky cross-stratification, suggesting they formed at or near the sediment-water interface. Finally, Mg-silicates in the lower Svanbergfjellet Formation are also preserved as a wide variety of coated grain lithofacies, similar to what is described above from the Callison Lake Formation.

On the Relationship Between Mg-Silicate and $CaCO_3$ Microspar Authigenesis

Tosca et al. (2011) provided experimental evidence for the mechanisms of Mg-silicate nucleation and crystallization from seawater-derived fluids, in which a primary amorphous Mg-silicate phase undergoes crystallization and maturation (accompanied by loss of structural H_2O) to generate sedimentary talc. Because talc (in addition to other Mg-silicates) is hydrophobic, its presence in aqueous systems would be predicted to generate immiscible textures; that is, physical separation of the liquid phase from the adjacent hydrophilic minerals. Consistent with this observation, nodules documented from the Svanbergfjellet Formation exhibit "oil-in-water" textures, where Mg-silicate nodules are surrounded by $CaCO_3$ microspar, as evidenced by the aggregation and physical separation of Mg-silicate crystallites from the surrounding microcrystalline $CaCO_3$ matrix (Fig. 2D-F, main text). This provides direct support that Mg-silicate nodules were initially precipitated as fine-grained crystallites in intimate contact with microcrystalline $CaCO_3$, and that they rapidly aggregated together in a $CaCO_3$ matrix that was fluid (and thus not fully lithified). In addition, this indicates that the Mg-silicates and $CaCO_3$ microspar precipitated contemporaneously, and that the two phases physically separated due to surface charge disparities. This is inconsistent with alternative models for nodule growth where the diffusion of components within the sediment either displaces or replaces the sediment matrix (in this case $CaCO_3$ microspar). On the contrary, the microspar matrix surrounding the Mg-silicates exhibits no evidence for displacement or replacement and is composed instead of euhedral, interlocking crystalline masses.

Although Tosca et al. (2011) initially interpreted the Mg-silicate precipitates as a wholly diagenetic phenomenon, their explanation is at odds with mass balance constraints, as well as geochemical and sedimentological data. First, as stated in the manuscript, the presence of pore-filling $CaCO_3$ microspar requires the delivery of significant amounts of seawater through the uppermost portion of the sediment. If we assume that seawater [Ca] was equivalent to ~10 mmol/kg (i.e., Spear et al., 2014), and assume that only 50% of the $CaCO_3$ microspar volume was originally precipitated (and the remaining 50% precipitated as a later overgrowth), a microspar-rich ribbon 7 x 5 x 1 cm in size requires more than 47 liters of seawater to form. This strongly supports the inference that synsedimentary $CaCO_3$ microspar cement, like any other syndepositional carbonate cement, reflects crystallization from seawater rather than diagenetic fluids, a conclusion reached by many previous authors, including Shields (2002), Bishop and Sumner (2006), and James et al. (1998). Bishop and Sumner (2006) proposed that large amounts of seawater could be injected into permeable and porous sediments through hydrostatic responses to wave oscillation (i.e., storms or normal wave activity above fair-weather wave base), which is consistent with the paleoenvironmental interpretation for the Svanbergfjellet Formation.

Previous studies of $CaCO_3$ microspar have also documented that microspar crystallization took place (1) before appreciable compaction of the sediment, and (2) while the sediment itself was susceptible to physical re-working. For example, the Svanbergfjellet Formation contains $CaCO_3$ microspar clasts and $CaCO_3$ microspar grainstone lags, which speaks to the erodibility of

the sediment shortly after the microspar precipitated. This phenomenon has also been observed in many $CaCO_3$ microspar-bearing successions (e.g., James et al., 1998).

A diagenetic origin for microspar $CaCO_3$ is inconsistent with geochemical observations on Tonian carbonate rocks in general (and the Svanbergfjellet Formation in particular). Although Tosca et al. (2011) noted that microbial sulfate reduction and microbial iron reduction are effective alkalinity pumps that could drive $CaCO_3$ supersaturation, the Svanbergfjellet carbonates, like many other examples (Grotzinger and James, 2000), are devoid of the metabolites produced by both of these processes. In other words, sedimentary Fe, in any form, as well as sulfur, are both conspicuously absent in these sediments, as is organic matter (e.g., Sperling et al., 2015; Kunzmann et al., 2017; Sperling and Stockey, 2018). Although oxic respiration of organic matter during diagenesis may influence the chemistry of pore waters and result in negligible organic matter preservation, this process consumes alkalinity rather than producing it, resulting in an overall pH decrease. These geochemical observations are also consistent with $\delta^{13}C$ analyses of microspar (e.g., Tracy and Lyons, 1998; Shields, 2002; Hodgskiss et al., 2018), which show no anomalous negative $\delta^{13}C$ fractionation, and are consistent with the $\delta^{13}C$ of contemporaneous carbonate sediments worldwide. Critically, the latter study by Hodgskiss et al. (2018) claimed that Fe reduction was a key process in creating enough alkalinity to generate molar tooth structures; however, the extreme sensitivity of the Fe isotope system to host phases was not explored in that study, which makes the isotopic results ambiguous. Together, mass balance constraints, in combination with geochemical and sedimentological observations, support the interpretation that pore-filling microspar cement reflects fluids dominated by contemporaneous seawater.

CARBONATE SYSTEM REACTION PATH MODELLING

In order to quantitatively examine the effects of variable alkalinity and $[Ca^{2+}]$ ratios in Neoproterozoic seawater on pH and mineralogy, we executed reaction path models of evaporation that take into account changing $CaCO_3$ solubility, CO_2 solubility, and aqueous carbonate speciation with increasing ionic strength. All evaporation models were performed with the Geochemist's Workbench v11.0 (Bethke and Yeakel, 2015) software using the Pitzer ion interaction model for calculating ion activity coefficients and mineral solubility upon evaporation (Pitzer, 1973; Harvie et al., 1984). Pitzer ion interaction parameters for the dissolved carbonate system, as well as apparent dissociation constants for $H_2CO_3^o$ and HCO_3^-, were taken from He & Morse (1993); however, in order to more realistically account for $CaCO_3$ precipitation from seawater-derived fluids, the apparent solubility of calcite in seawater was taken from Mucci (1983). Because the solubility products of aragonite and calcite are similar to one another, the choice of $CaCO_3$ polymorph has no discernible effect on the subsequent evolution of evaporating fluids. We chose calcite as the polymorph for modelling calculations here, acknowledging that either aragonite or calcite (or both) may have been dominant $CaCO_3$ phases precipitating from Neoproterozoic seawater or its derivatives. Evaporation models were run by specifying equilibrium between atmospheric CO_2 and dissolved carbonate species in solution (Lazar et al., 1983). Back reaction between minerals and the evolving fluid was permitted. All simulations begin with concentrations for Na^+, K^+, Mg^{2+}, Cl^-, and SO_4^{2-} constrained by Spear et al. (2014). Atmospheric CO_2 concentration (and therefore total alkalinity), pH, and Ca^{2+} concentrations were adjusted to examine situations where $2*[Ca^{2+}]$ was less than or greater than the total alkalinity, keeping estimates of these parameters consistent with constraints presented the main text.

The results of the modelling simulations show that the pH threshold of 8.5, required to nucleate Mg-silicate directly from Neoproterozoic seawater (Tosca et al., 2011), is only crossed

when [ALK] > 2*[Ca^{2+}]. Under these conditions (Fig. DR2), pH increases to a maximum value of 8.62, and remains above pH 8.5 during and after $CaCO_3$ precipitation and through the precipitation of halite (NaCl). When [Ca^{2+}] is quantitatively consumed by $CaCO_3$ precipitation under these conditions, gypsum ($CaSO_4 \cdot 2H_2O$) is not predicted as a significant direct precipitate from water (Fig. DR3); however, modelling results show that late-stage evaporation leads to the precipitation of anhydrite and, in some cases, the back-reaction of $CaCO_3$ and the subsequent formation of gypsum or anhydrite. This implies that gypsum and/or anhydrite ($CaSO_4$) are not exclusively prohibited from forming in systems where [ALK] > 2*[Ca^{2+}], which is consistent with sedimentological observations from the Callison Lake Formation (Strauss et al., 2015). $CaCO_3$ back-reaction is due to the effect of calcite solubility changes with increasing evaporation and the subsequent release of Ca^{2+} which can promote gypsum precipitation. These late-stage effects are also consistent with studies of Lazar et al. (1983) and McCaffrey et al. (1987), but it is worth noting that other geochemical factors may also influence the presence or absence of gypsum/anhydrite formation, as well as the concentration factor associated with its formation. For example, increases in [SO_4^{2-}] beyond the 3 mmol/kg used here (Spear et al., 2014) result in earlier and more abundant gypsum/anhydrite precipitation, independent of the relationship between [ALK] and [Ca^{2+}].

Reaction path modelling results for Tonian seawater confirm that when [ALK] < 2*[Ca] (Fig. DR2), pH decreases upon calcite precipitation, similar to modern seawater (Krumgalz et al., 1980; Lazar et al., 1983; McCaffrey et al., 1987). Under these conditions, the bulk mineralogy includes calcite, gypsum, halite, and late stage chloride salts. The modelling results show that when Ca^{2+} is not qualitatively depleted by $CaCO_3$ precipitation, gypsum and halite precipitation occur almost simultaneously at concentration factors of approximately 10x, which is consistent with constraints from Spear et al. (2014). Building upon the results of these constraints, we performed carbonate chemistry calculations using custom scripts written in MATLAB for both the Callison Lake Formation (Fig. DR4) and Svanbergfjellet Formation (Fig. DR5), which are described further in the main text.

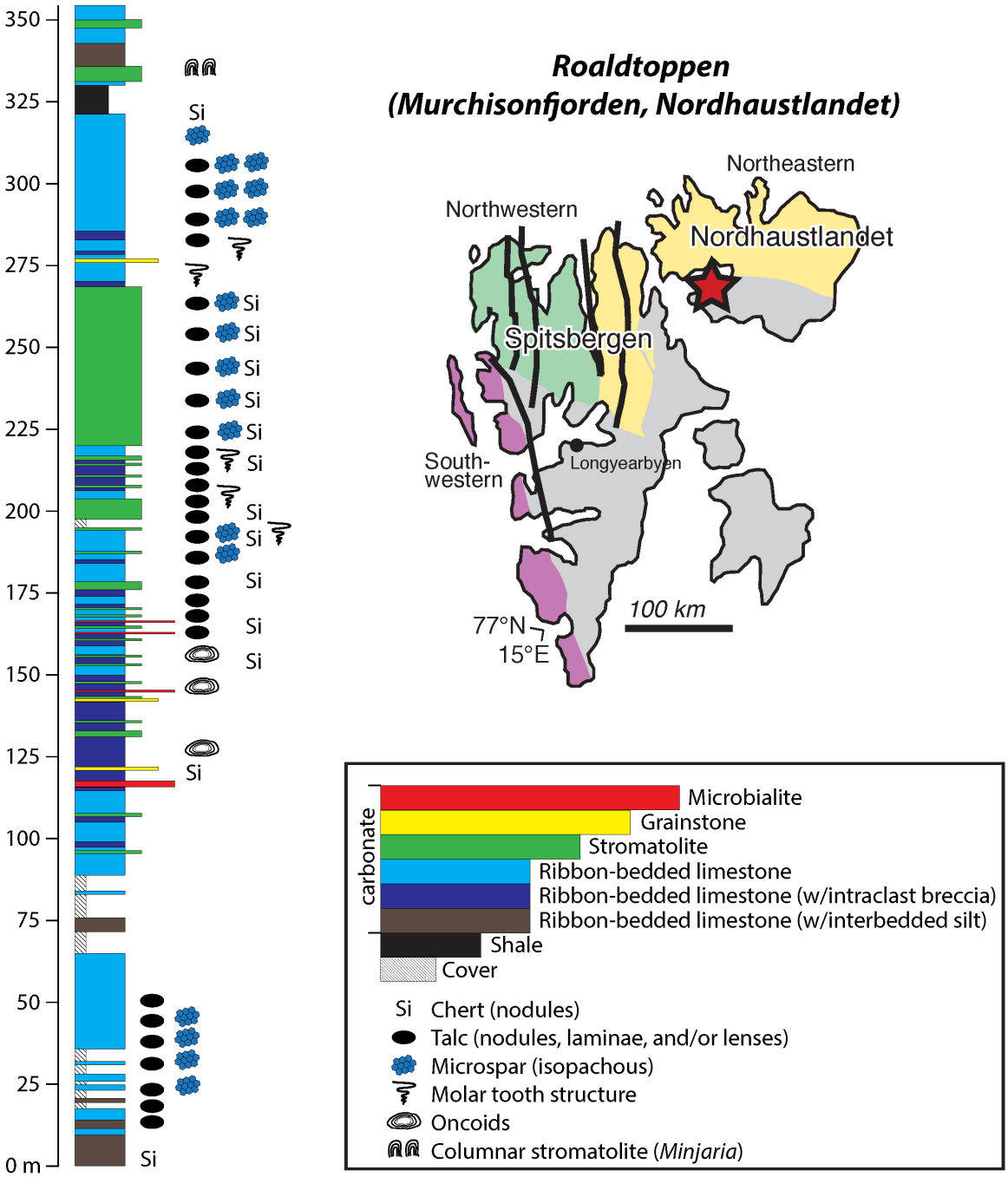

Figure DR1. Measured section (**left**) of the lower Svanbergfjellet Formation (Lower Dolomite Member) from Roaldtoppen, Murchisonfjorden, Nordhaustlandet, Svalbard. Inset map (**upper right**) shows the location of the measured section (red star) and legend (**lower right**) describes the main observed lithofacies within the measured section. Note the widespread occurrence of Mg-silicates (talc) and $CaCO_3$ microspar throughout the measured section. Petrographic thin sections presented in Fig. 2 of the main text are from ~175-180 m in the measured section.

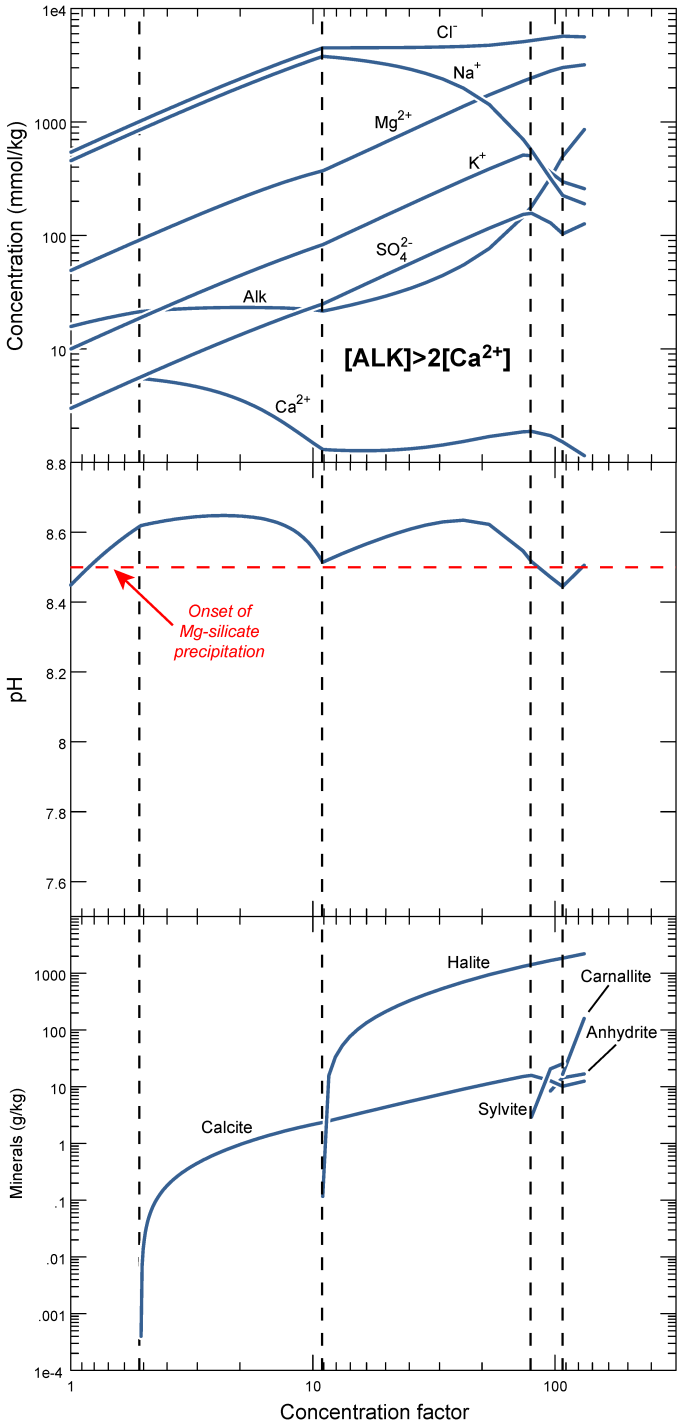

Figure DR2. Reaction path model outputs for the evaporation of Neoproterozoic seawater (based on the composition reported in Spear et al., 2014) where [ALK] > 2*[Ca^{2+}]. Under these conditions, Ca^{2+} is rapidly consumed during chemically induced $CaCO_3$ precipitation and residual alkalinity increases with evaporation (**top**), resulting in a sustained increase in pH (**middle**). The onset of Mg-silicate precipitation, at pH 8.5, is reached close to the onset of $CaCO_3$ precipitation in this example, but well before halite precipitation (**bottom**). pH continues to increase to a maximum of 8.62.

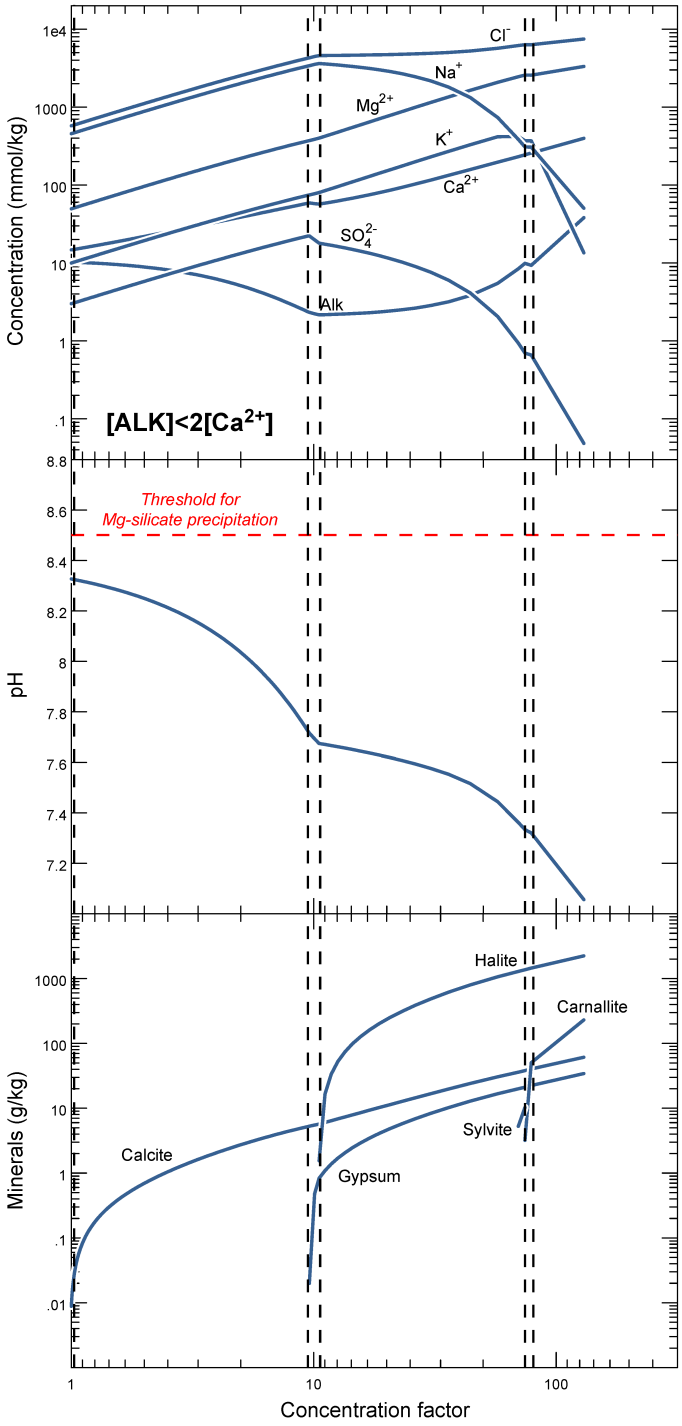

Figure DR3. Reaction path model outputs for evaporation of Neoproterozoic seawater (based on the composition reported in Spear et al., 2014) where [ALK] < 2*[Ca^{2+}]. Under these conditions, [ALK] is largely consumed through chemically induced $CaCO_3$ precipitation (**top**), which results in a decrease in pH (**middle**). Gypsum and halite both precipitate at concentration factors of ~10 (**bottom**), in close agreement with calculations presented by Spear et al. (2014).

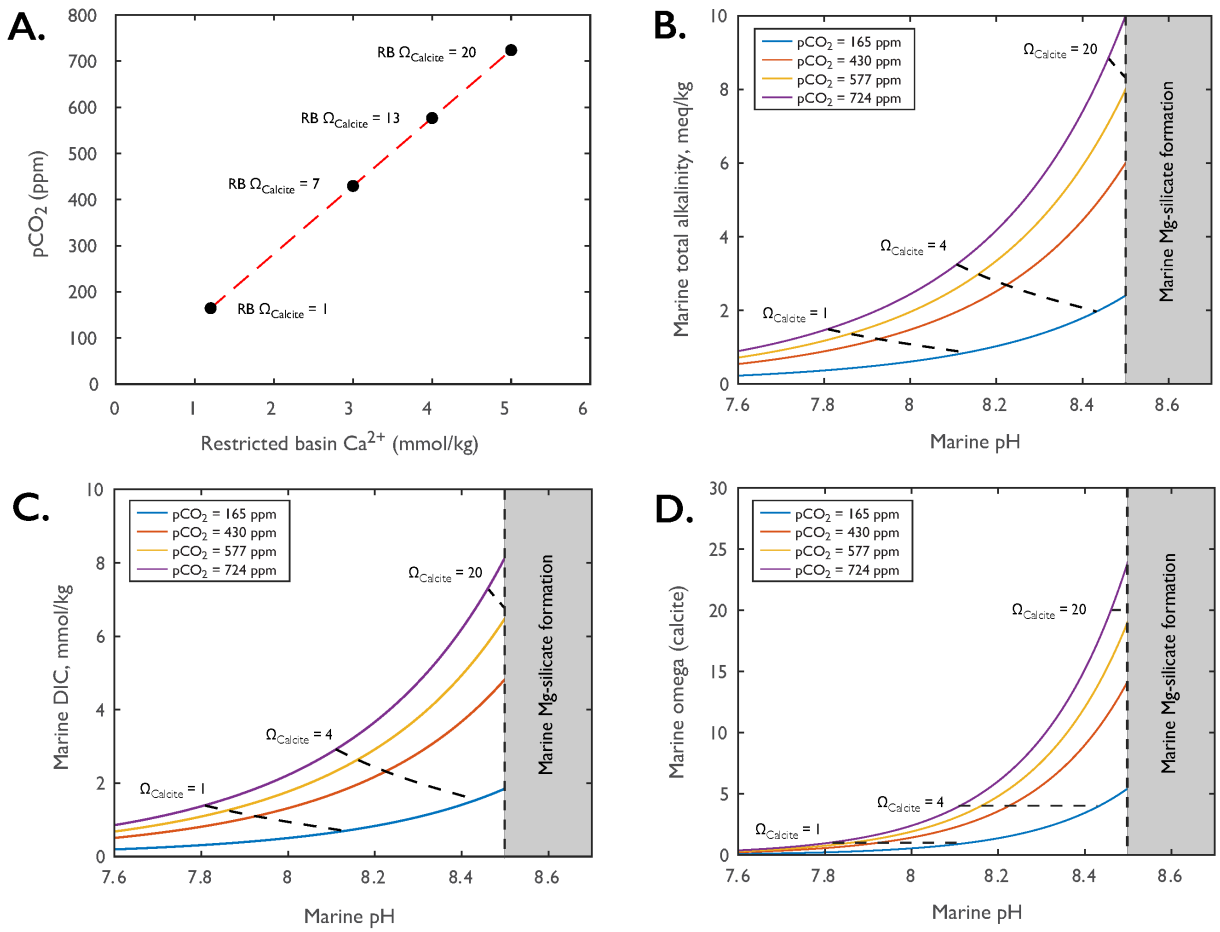

Figure DR4. Tonian carbonate equilibrium constraints derived from the ca. 755–735 Ma Callison Lake depositional system. **A**) Plot of pCO_2 vs. [Ca^{2+}] for the Callison Lake restricted basin (RB) at different $\Omega_{Calcite}$ values. **B**) Plot of total marine alkalinity vs. pH for open marine systems at the time of Callison Lake deposition at different $\Omega_{Calcite}$ and pCO_2 values. **C)** Plot of total marine DIC vs. pH for open marine systems at the time of Callison Lake deposition at different $\Omega_{Calcite}$ and pCO_2 values. **D)** Plot of marine $\Omega_{Calcite}$ vs. pH for open marine systems at the time of Callison Lake deposition at different pCO_2 values. In **A–D**, the grey area defines a chemical space where marine pH would be above the critical supersaturation level for Mg-silicate authigenesis.

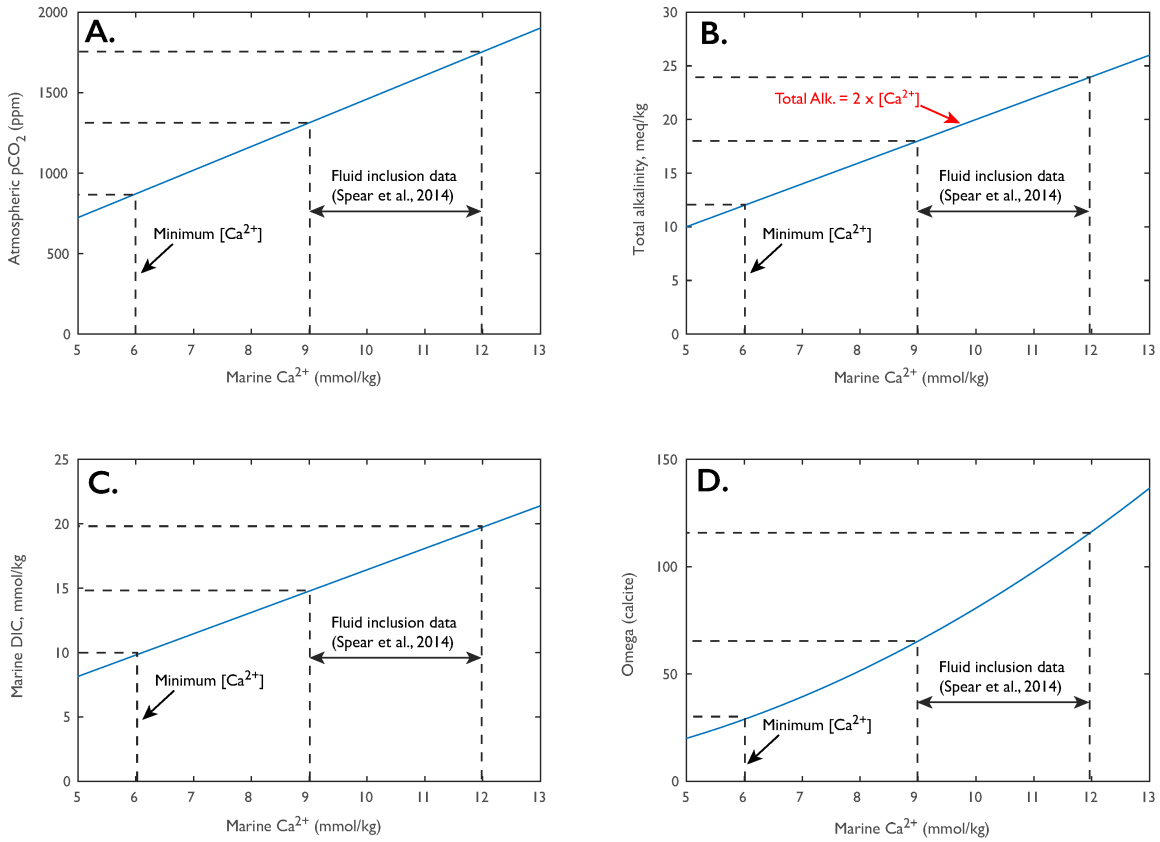

Figure DR5. Tonian carbonate equilibrium constraints derived from the ca. 805–788 Ma Svanbergfjellet Formation. **A**) Plot of atmospheric pCO_2 vs. $[Ca^{2+}]$ for the Svanbergfjellet Formation based on calculated Tonian $[Ca^{2+}]$ = 6-12 mmol/kg from Spear et al. (2014) and minimum from evaporation modeling. **B)** Plot of total marine alkalinity vs. $[Ca^{2+}]$ for the Svanbergfjellet Formation. **C)** Plot of marine DIC vs. $[Ca^{2+}]$ for the Svanbergfjellet Formation. **D)** Plot of $\Omega_{Calcite}$ vs. $[Ca^{2+}]$ for the Svanbergfjellet Formation.

REFERENCES CITED

Bethke, C.M., and Yeakel, S., 2015, GWB Essentials Guide. Aqueous Solutions: LLC Champaign, Illinois, USA.

Calver, C.R., Crowley, J.L., Wingate, M.T.D., Evans, D.A.D., Raub, T.D., and Schmitz, M.D., 2013, Globally synchronous Marinoan deglaciation indicated by U-Pb geochronology of the Cottons Breccia, Tasmania, Australia: Geology, v. 41, p. 1127–1130, doi:10.1130/G34568.1.

Cohen, P.A., Irvine, S.W., and Strauss, J.V., 2017a, Vase-shaped microfossils from the Tonian Callison Lake Formation of Yukon, Canada: taxonomy, taphonomy and stratigraphic palaeobiology (H. Coxall, Ed.): Palaeontology, v. 60, p. 683–701, doi:10.1111/pala.12315.

Cohen, P.A., Strauss, J.V., Rooney, A.D., Sharma, M., and Tosca, N.J., 2017b, Controlled hydroxyapatite biomineralization in an ~810 million-year-old unicellular eukaryote: *Science Advances*, v. 3, n. 6, p. 1-8.

Condon, D., 2005, U-Pb Ages from the Neoproterozoic Doushantuo Formation, China: Science, v. 308, p. 95–98, doi:10.1126/science.1107765.

Dallmann, W.K. (Ed.), 2015, Geoscience Atlas of Svalbard: Tromsø, Norway, Norwegian Polar Institute, Norwegian Polar Institute Report Series 148, 292 p.

Gee, G., Hjelle, A., Siggerud, T., and Winsnes, T.S. The geology of Nordaustlandet, northern and central parts: , p. 145.

Halverson, G.P., Maloof, A.C., and Hoffman, P.F., 2004, The Marinoan glaciation (Neoproterozoic) in northeast Svalbard: Basin Research, v. 16, p. 297–324, doi:10.1111/j.1365-2117.2004.00234.x.

Halverson, G.P., Maloof, A.C., Schrag, D.P., Dudás, F.Ö., and Hurtgen, M., 2007, Stratigraphy and geochemistry of a ca 800 Ma negative carbon isotope interval in northeastern Svalbard: Chemical Geology, v. 237, p. 5–27, doi:10.1016/j.chemgeo.2006.06.013.

Halverson, G.P., Kunzmann, M., Strauss, J.V., and Maloof, A.C., 2018a, The Tonian-Cryogenian transition in Northeastern Svalbard: Precambrian Research, v. 319, p. 79–95, doi:10.1016/j.precamres.2017.12.010.

Halverson, G.P., Porter, S.M., and Gibson, T.M., 2018b, Dating the late Proterozoic stratigraphic record: Emerging Topics in Life Sciences, v. 2, p. 137–147, doi:10.1042/ETLS20170167.

Harland, W.B., Hambrey, M.J., and Waddams, 1993, Vendian Geology of Svalbard: Oslo, Norsk Polarinstitutt, Skrifter / Norsk Polarinstitutt 193, 68 p.

Harland, W.B., and Wilson, C.B., 1956, The Hecla Hoek Succession in Ny Friesland, Spitsbergen: Geological Magazine, v. 93, p. 265–286, doi:10.1017/S0016756800066693.

Harvie, C.E., Møller, N., and Weare, J.H., 1984, The prediction of mineral solubilities in natural waters: The Na-K-Mg-Ca-H-Cl-SO_4-OH-HCO_3-CO_3-CO_2-H_2O system to high ionic strengths at 25°C: Geochimica et Cosmochimica Acta, v. 48, p. 723–751.

He, S., and Morse, J.W., 1993, The carbonic acid system and calcite solubility in aqueous Na-K-Ca-Mg-Cl-SO4 solutions from 0 to 90 C: Geochimica et Cosmochimica Acta, v. 57, p. 3533–3554.

Hodgskiss, M.S., Kunzmann, M., Poirier, A. and Halverson, G.P., 2018. The role of microbial iron reduction in the formation of Proterozoic molar tooth structures: Earth and Planetary Science Letters, v. 482, p.1-11.

Hoffman, P.F., Halverson, G.P., Domack, E.W., Maloof, A.C., Swanson-Hysell, N.L., and Cox, G.M., 2012, Cryogenian glaciations on the southern tropical paleomargin of Laurentia (NE Svalbard and East Greenland), and a primary origin for the upper Russøya (Islay) carbon isotope excursion: Precambrian Research, v. 206–207, p. 137–158, doi:10.1016/j.precamres.2012.02.018.

Hoffmann, K.-H., Condon, D.J., Bowring, S.A., and Crowley, J.L., 2004, U-Pb zircon date from the Neoproterozoic Ghaub Formation, Namibia: Constraints on Marinoan glaciation: Geology, v. 32, p. 817, doi:10.1130/G20519.1.

Knoll, A.H., 1984, Microbiotas of the Late Precambrian Hunnberg Formation, Nordaustlandet, Svalbard: Journal of Paleontology, v. 58, p. 131–162.

Knoll, A.H., and Swett, K., 1990, Carbonate deposition during the late Proterozoic Era: an example from Spitsbergen.: American journal of science, v. 290-A, p. 104–132.

Krumgalz, B.S., Hornung, H., and Oren, O.H., 1980, The study of a natural hypersaline lagoon in a desert area (the Bardawil Lagoon in northern Sinai): Estuarine and Coastal Marine Science, v. 10, p. 403–415.

Lazar, B., Starinsky, A., Katz, A., Sass, E., and work(s):, S.B.-Y.R., 1983, The Carbonate System in Hypersaline Solutions: Alkalinity and $CaCO_3$ Solubility of Evaporated Seawater: Limnology and Oceanography, v. 28, p. 978–986.

Macdonald, F.A., Schmitz, M.D., Crowley, J.L., Roots, C.F., Jones, D.S., Maloof, A.C., Strauss, J.V., Cohen, P.A., Johnston, D.T., and Schrag, D.P., 2010, Calibrating the Cryogenian: Science, v. 327, p. 1241–1243, doi:10.1126/science.1183325.

Macdonald, F.A., Schmitz, M.D., Strauss, J.V., Halverson, G.P., Gibson, T.M., Eyster, A., Cox, G., Mamrol, P., and Crowley, J.L., 2018, Cryogenian of Yukon: Precambrian Research, v. 319, p. 114–143, doi:10.1016/j.precamres.2017.08.015.

MacLennan, S., Park, Y., Swanson-Hysell, N., Maloof, A., Schoene, B., Gebreslassie, M., Antilla, E., Tesema, T., Alene, M., and Haileab, B., 2018, The arc of the Snowball: U-Pb dates constrain the Islay anomaly and the initiation of the Sturtian glaciation: Geology, v. 46, p. 539–542, doi:10.1130/G40171.1.

Maloof, A.C., Halverson, G.P., Kirschvink, J.L., Schrag, D.P., Weiss, B.P., and Hoffman, P.F., 2006, Combined paleomagnetic, isotopic, and stratigraphic evidence for true polar wander from the Neoproterozoic Akademikerbreen Group, Svalbard, Norway: Geological Society of America Bulletin, p. 26.

McCaffrey, M.A., Lazar, B., and Holland, H.D., 1987, The evaporation path of seawater and the coprecipitation of Br (super-) and K (super+) with halite: Journal of Sedimentary Research, v. 57, p. 928–937.

Mucci, A., 1983, The solubility of calcite and aragonite in seawater at various salinities, temperatures, and one atmosphere total pressure: American Journal of Science, v. 283, p. 780–799.

Pitzer, K.S., 1973, Thermodynamics of electrolytes. I. Theoretical basis and general equations: The Journal of Physical Chemistry, v. 77, p. 268–277.

Rooney, A.D., Macdonald, F.A., Strauss, J.V., Dudas, F.O., Hallmann, C., and Selby, D., 2014, Re-Os geochronology and coupled Os-Sr isotope constraints on the Sturtian snowball Earth: Proceedings of the National Academy of Sciences, v. 111, p. 51–56, doi:10.1073/pnas.1317266110.

Rooney, A.D., Strauss, J.V., Brandon, A.D., and Macdonald, F.A., 2015, A Cryogenian chronology: Two long-lasting synchronous Neoproterozoic glaciations: Geology, v. 43, p. 459–462, doi:10.1130/G36511.1.

Spear, N., Holland, H.D., Garcia-Veígas, J., Lowenstein, T.K., Giegengack, R., and Peters, H., 2014, Analyses of fluid inclusions in Neoproterozoic marine halite provide oldest measurement of seawater chemistry: Geology, v. 42, p. 103–106, doi:10.1130/G34913.1.

Strauss, J.V., Macdonald, F.A., Halverson, G.P., Tosca, N.J., Schrag, D.P., and Knoll, A.H., 2015, Stratigraphic evolution of the Neoproterozoic Callison Lake Formation: Linking the break-up of Rodinia to the Islay carbon isotope excursion: American Journal of Science, v. 315, p. 881–944, doi:10.2475/10.2015.01.

Strauss, J.V., Rooney, A.D., Macdonald, F.A., Brandon, A.D., and Knoll, A.H., 2014, 740 Ma vase-shaped microfossils from Yukon, Canada: Implications for Neoproterozoic chronology and biostratigraphy: Geology, v. 42, p. 659–662, doi:10.1130/G35736.1.

Swanson-Hysell, N.L., Maloof, A.C., Condon, D.J., Jenkin, G.R.T., Alene, M., Tremblay, M.M., Tesema, T., Rooney, A.D., and Haileab, B., 2015, Stratigraphy and geochronology of the Tambien Group, Ethiopia: Evidence for globally synchronous carbon isotope change in the Neoproterozoic: Geology, v. 43, p. 323–326, doi:10.1130/G36347.1.

Tosca, N.J., Macdonald, F.A., Strauss, J.V., Johnston, D.T., and Knoll, A.H., 2011, Sedimentary talc in Neoproterozoic carbonate successions: Earth and Planetary Science Letters, v. 306, p. 11–22, doi:10.1016/j.epsl.2011.03.041.

356 Wilson, C.B., 1958, The Lower Middle Hecla Hoek Rocks of Ny Friesland, Spitsbergen:
357 Geological Magazine, v. 95, p. 305–327, doi:10.1017/S0016756800062865.

358 Wilson, C.B., 1961, The Upper Middle Hecla Hoek Rocks of Ny Friesland, Spitsbergen:
359 Geological Magazine, v. 98, p. 89–116, doi:10.1017/S0016756800060325.